LETTERS
PUBLISHED ONLINE: 5 AUGUST 2012 | DOI: 10.1038/NCLIMATE1633
nature climate change

Increasing drought under global warming in observations and models

Aiguo Dai

Historical records of precipitation, streamflow and drought indices all show increased aridity since 1950 over many land areas[1,2]. Analyses of model-simulated soil moisture[3,4], drought indices[1,5,6] and precipitation-minus-evaporation[7] suggest increased risk of drought in the twenty-first century. There are, however, large differences in the observed and model-simulated drying patterns[1,2,6]. Reconciling these differences is necessary before the model predictions can be trusted. Previous studies[8–12] show that changes in sea surface temperatures have large influences on land precipitation and the inability of the coupled models to reproduce many observed regional precipitation changes is linked to the lack of the observed, largely natural change patterns in sea surface temperatures in coupled model simulations[13]. Here I show that the models reproduce not only the influence of El Niño-Southern Oscillation on drought over land, but also the observed global mean aridity trend from 1923 to 2010. Regional differences in observed and model-simulated aridity changes result mainly from natural variations in tropical sea surface temperatures that are often not captured by the coupled models. The unforced natural variations vary among model runs owing to different initial conditions and thus are irreproducible. I conclude that the observed global aridity changes up to 2010 are consistent with model predictions, which suggest severe and widespread droughts in the next 30–90 years over many land areas resulting from either decreased precipitation and/or increased evaporation.

Although the historical and future aridity changes have been discussed in previous studies[1–7], there still is a need to validate the historical changes and reconcile them with model projections. Here I focus on synthesizing the observed aridity changes and comparing and reconciling them with model-simulated changes, thereby improving our understanding of global-warming-induced drought changes.

Different drought indices can result in somewhat different change patterns, especially on small scales[14]. Here I focus on the large-scale drying trends in precipitation, streamflow and soil moisture fields, which are commonly used to quantify, respectively, meteorological, hydrologic and agricultural drought[1]. Because historical records of soil moisture are sparse, I also used the self-calibrated Palmer drought severity index (PDSI) with potential evapotranspiration estimated using the Penman–Monteith equation (sc_PDSI_pm; ref. 2). The PDSI is calculated from a water-balance model forced with observed precipitation and temperature and has been widely used in monitoring drought development over the USA, palaeoclimate reconstruction[15] and studying aridity changes[2,5,6,16]. The revised sc_PDSI_pm has improved spatial comparability and uses a more realistic estimate of potential evapotranspiration, thus improving its applicability to global warming scenarios (see ref. 2 for more details).

Figure 1a,b shows that the broad patterns of the linear trends from 1950 to 2010 in observed annual precipitation and calculated sc_PDSI_pm using observation-based forcing[2] are comparable. These patterns are also broadly comparable to those seen in observed streamflow trends since 1948 in the world's main river basins[1,17]. Some regional and quantitative differences are expected among them as they are different variables, albeit closely related physically. The patterns are characterized by drying over most of Africa, southeast Asia, eastern Australia and southern Europe, and increased wetness over the central US, Argentina and northern high-latitude areas. As the precipitation and streamflow data are from independent measurements, the broad consistency among their change patterns suggests that these trends are real. This also suggests that the sc_PDSI_pm is a useful measure of aridity changes. One advantage of the sc_PDSI_pm is that it can be used to examine the impact of individual forcing on the aridity trend by comparing the cases with and without this forcing in calculations of the sc_PDSI_pm. Figure 1c shows that the warming since the 1980s (note the jump around the early 1980s is due to the 1982/1983 El Niño) has contributed considerably to the upward trend in global drought areas, increasing the areas under drought by about 8% by the first decade of this century. This warming-induced drying results from increased evaporation and is largest over northern mid-high latitudes[2]. In contrast, precipitation decreases over Africa, southeast Asia, eastern Australia and southern Europe are the primary cause for the drying trend over there, and the long-term trends and decadal to multidecadal variations in sea surface temperature (SST) are a major driver for many of the precipitation changes[8–12]. The long-term SST trend is part of the global warming; however, many of the observed decadal to multidecadal SST variations are absent in greenhouse-gas- (GHG) and aerosol-forced coupled model simulations[13], implying that these SST variations are unforced, natural variations whose phase or timing and spatial patterns may depend on the initial conditions of the models and thus they are generally irreproducible.

To study how drought might change under increasing GHGs, I analysed coupled climate model simulations under intermediate future GHG emissions scenarios from the Coupled Model Intercomparison Project phase 3 (CMIP3) and the new phase 5 (CMIP5). The sc_PDSI_pm maps for future decades based on the CMIP3 were briefly discussed in ref. 1, but were not compared with the simulated soil-moisture and historical sc_PDSI_pm changes. Figure 2a shows that most (more than 82%) of the 14 CMIP5 models analysed here show decreases in soil-moisture content in the top-10 cm

National Center for Atmospheric Research, PO Box 3000, Boulder, Colorado 80307-3000, USA. The National Center for Atmospheric Research is sponsored by the US National Science Foundation. Address from 1 September 2012: Department of Atmospheric and Environmental Sciences, University at Albany, 1400 Washington Avenue, Albany, New York 12222, USA. e-mail: adai@ucar.edu; adai@albany.edu.

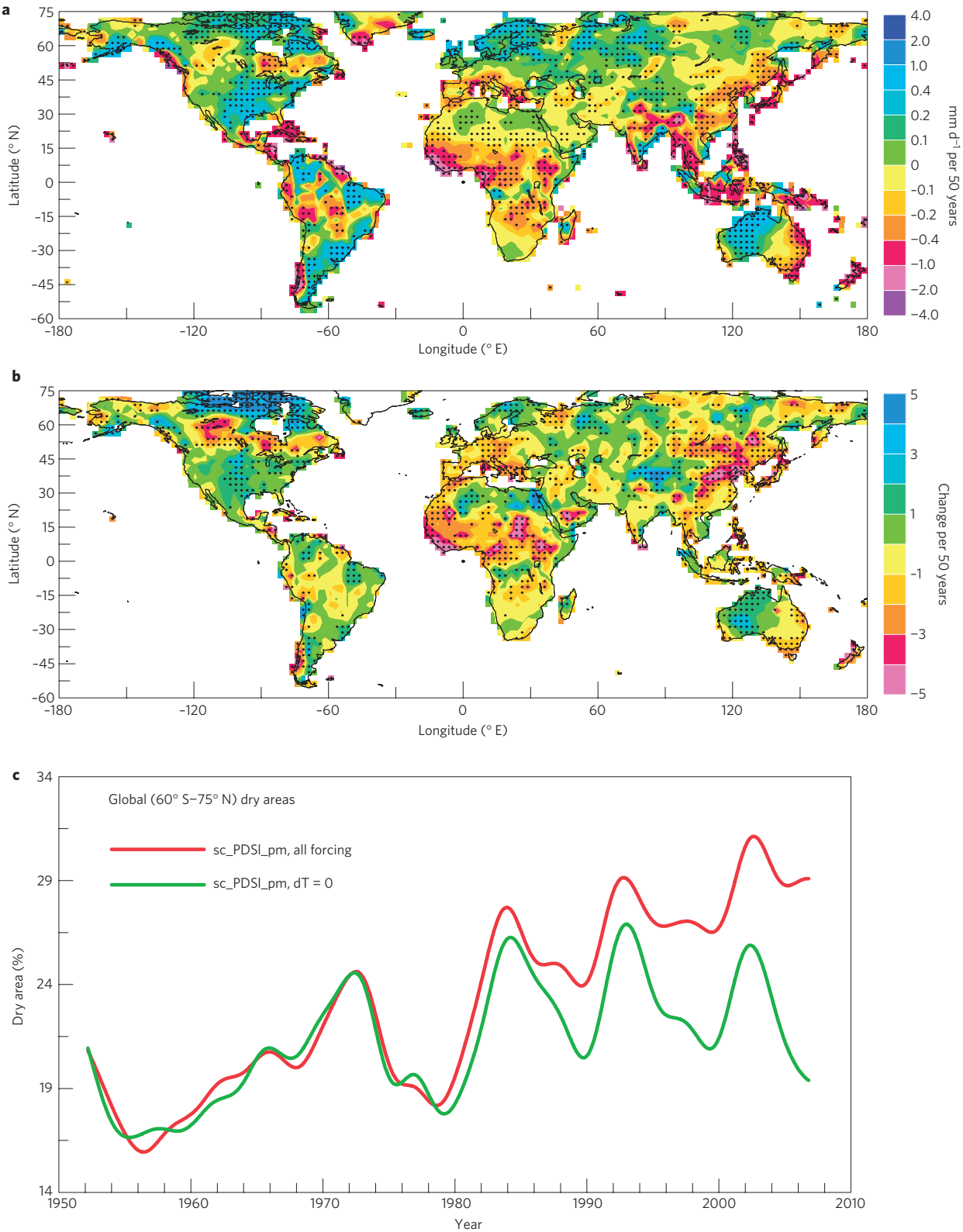

Figure 1 | Trend maps for precipitation and sc_PDSI_pm and time series of percentage dry areas. Long-term trends from 1950 to 2010 in annual mean **a**, observed precipitation[2] and **b**, calculated sc_PDSI_pm using observation-based forcing[2]. The stippling indicates the trend is statistically significant at the 5% level, with the effective degree of freedom computed using the method of ref. 30. Note a change of 0.5 in the sc_PDSI_pm is significant in the sense that a value of PDSI between −0.5 to −1.0, −1.0 to −2.0, −2.0 to −3.0 and −3.0 to −4.0 indicates, respectively, a dry spell, mild drought, moderate drought and severe drought[2]. **c**, Smoothed time series of the drought area as a percentage of global land areas based on the sc_PDSI_pm computed with (red line) and without (green line) the observed surface warming. The drought areas are defined locally as the cases when sc_PDSI_pm is below the value of the twentieth percentile of the 1950–1979 period (results are similar for drought defined as PDSI < −2.0 and for using a longer base period from 1948 to 2010).

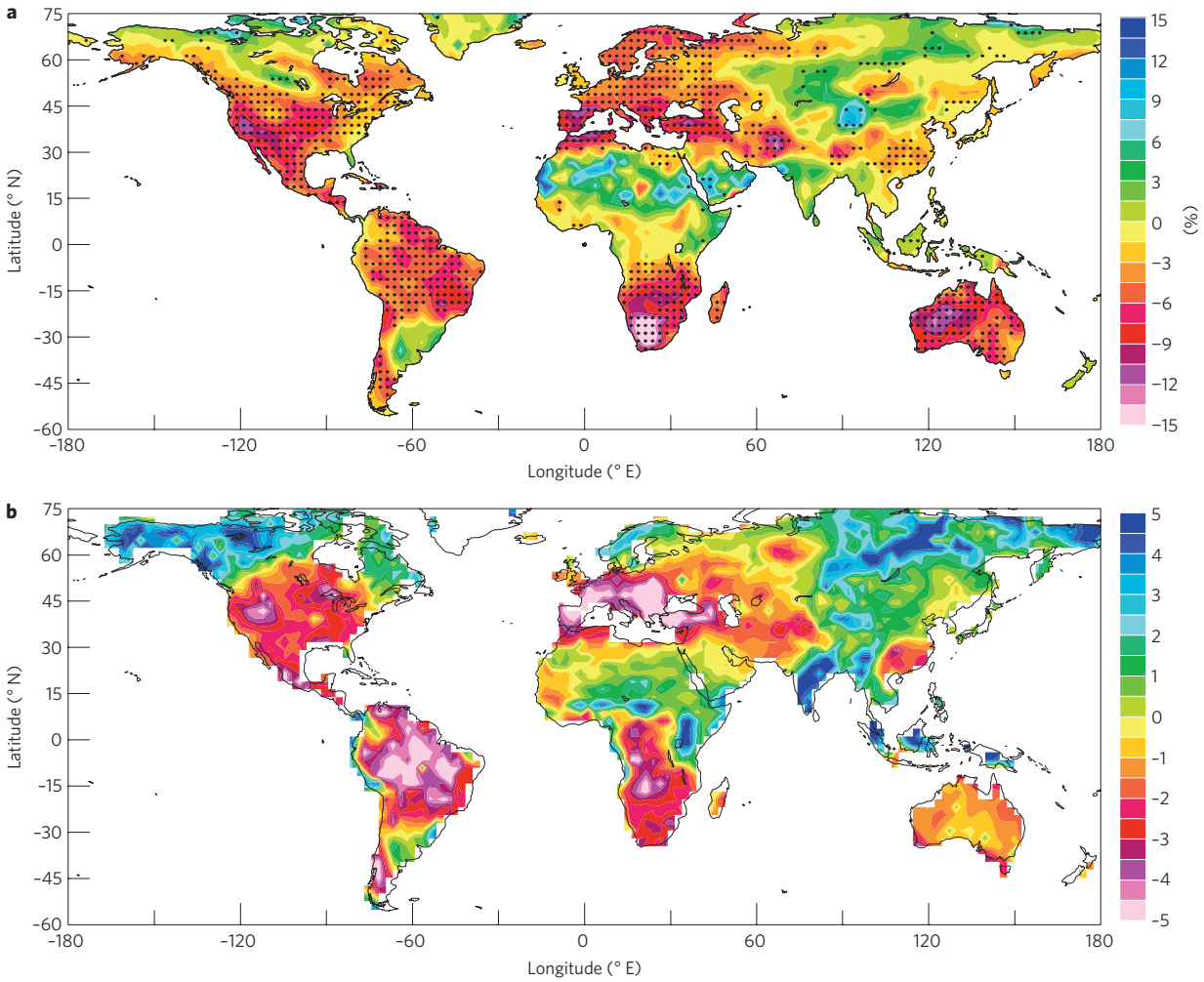

Figure 2 | Future changes in soil moisture and sc_PDSI_pm. a, Percentage changes from 1980–1999 to 2080–2099 in the multimodel ensemble mean soil-moisture content in the top 10 cm layer (broadly similar for the whole soil layer) simulated by 11 CMIP5 models under the RCP4.5 emissions scenario. Stippling indicates at least 82% (9 out of 11) of the models agree on the sign of change. **b**, Mean sc_PDSI_pm averaged over 2090–2099 computed using the 14-model ensemble mean climate (including surface air temperature, precipitation, wind speed, specific humidity and net radiation) from the CMIP5 simulations under the RCP4.5 scenario. A sc_PDSI_pm value of −3.0 or below indicates severe to extreme droughts for the present climate, but its quantitative interpretation for future values in **b** may require modification.

layer during the twenty-first century over most of the Americas, Europe, southern Africa, most of the Middle East, southeast Asia and Australia. The multimodel mean suggests decreases ranging from 5 to 15% by 2080–2099. The drying in the soil-moisture field is largely reproduced by the sc_PDSI_pm calculated using the same multimodel mean climate, although the sc_PDSI_pm suggests larger increases in wetness over central and eastern Asia and northern North America (Fig. 2b). Similar changes (but with some regional differences) are also seen in CMIP3 models[3,4] (Supplementary Fig. S1) and in all seasons (Supplementary Fig. S2).

As SSTs have large influences on land precipitation and drought, here I carried out a maximum covariance analysis[18] (MCA) of global fields of SSTs (40° S–60° N) and sc_PDSI_pm (60° S–75° N) from both observations and the CMIP models (also done for SST versus soil moisture for the model data). The goal is to examine whether the models can reproduce the observed relationship revealed by the leading MCA modes between SST and sc_PDSI_pm and whether the models can simulate the recent drying trend. By focusing on the leading MCA modes, many (but not all) of the unforced, irreproducible natural variations are excluded in such comparison.

Figure 3 shows that the second MCA modes (MCA2) from observations and the models are remarkably similar in spatial patterns. They both represent the variations induced by the El Niño-Southern Oscillation (ENSO), as the SST patterns (Fig. 3b,d) resemble the typical ENSO-induced SST anomaly patterns[12] and the temporal coefficient is highly correlated ($r = 0.87$) with an ENSO index (Fig. 3a). There are substantial decadal to multidecadal variations in this ENSO mode from observations as noticed previously[19], with the recent period since about 1999 becoming cooler in the central and eastern Pacific than the previous period from 1977 to 1998 (Fig. 3a,b). For the MCA2, we focus on the similarity in the spatial patterns between the observations and models, as the temporal coefficient for the multimodel ensemble mean (not shown) should bear little resemblance to the observed temporal evolution, which is realization dependent. The impact of ENSO on drought is reflected by the MCA2 for the sc_PDSI_pm, whose patterns (Fig. 3c,e) largely resemble those of ENSO-induced precipitation[20], with drier conditions over Australia, south Asia, northern South America, the Sahel and southern Africa and wetter conditions over the continental USA, Argentina, southern Europe and southwestern Asia in El Niño years.

Figure 4 shows that the first leading MCA modes (MCA1) from observations and the models represent the global warming, as the temporal coefficient is correlated strongly ($r = 0.97$) with

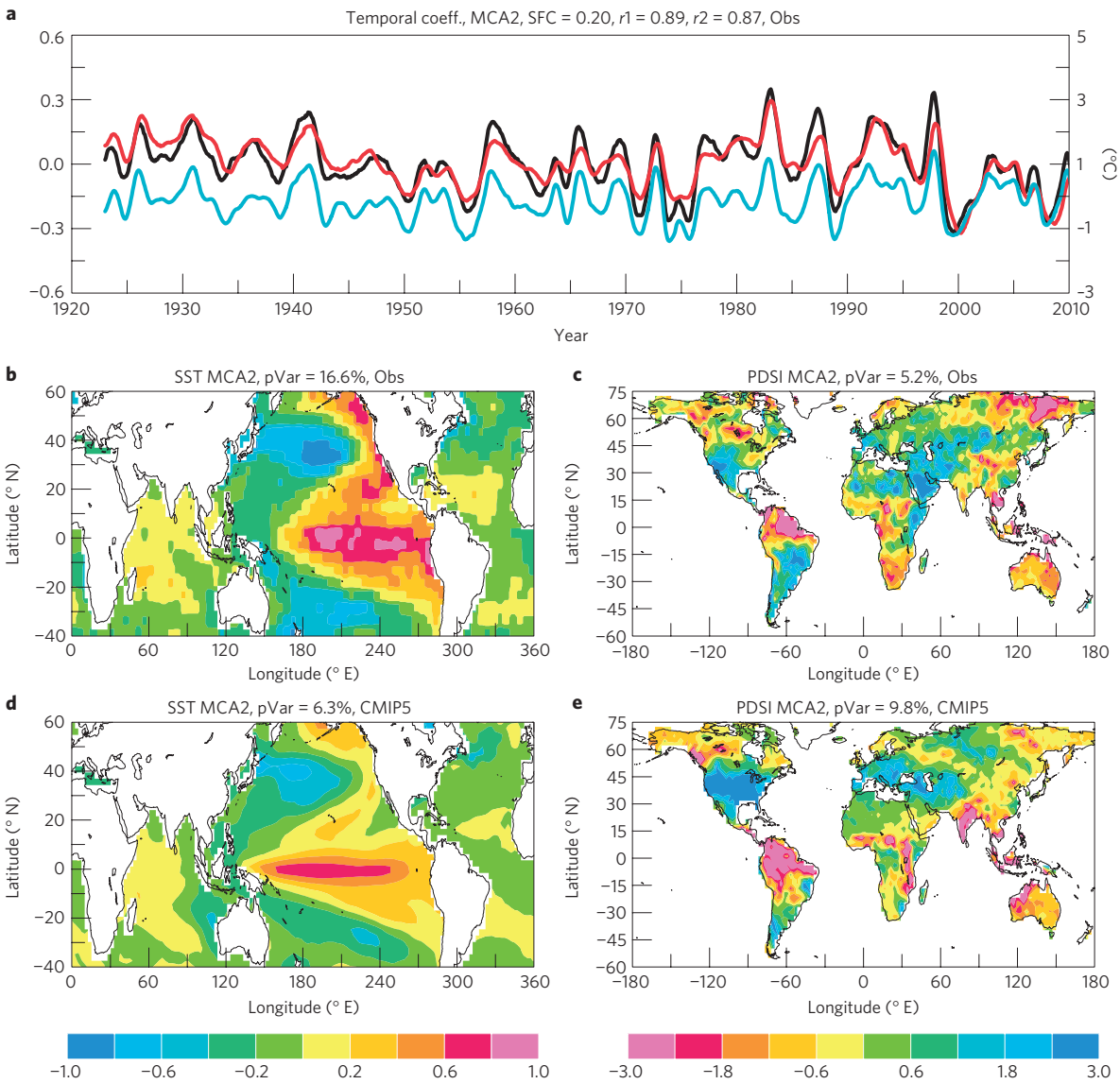

Figure 3 | Temporal and spatial patterns of the MCA2 mode for SST and sc_PDSI_pm from observations and models. a, Temporal (black line for SST, red line for sc_PDSI_pm, on the left-side ordinate) and **b**–**e**, spatial expansion coefficients of the second leading mode from a MCA of 13-point moving-averaged monthly SST from observations[27] and sc_PDSI_pm computed from observational forcing (**a**–**c**) and from 14 CMIP5 model ensemble-mean simulations (**d**,**e**) for 1923–2010 (observational data are unreliable for earlier years). The blue line in **a** is the observed Nino3.4 SST index (right-side ordinate) obtained from http://www.esrl.noaa.gov/psd/forecasts/sstlim/Globalsst.html (for 1950–2010) and from http://www.cgd.ucar.edu/cas/catalog/climind/TNI_N34/index.html#Sec5 (for pre-1950 years, rescaled to match the National Oceanic and Atmospheric Administration index over the 1950–2007 common data period). In **a**, SFC is the squared fractional covariance explained by the MCA mode and the *r*1 and *r*2 are the correlation coefficients between, respectively, the black and red, and the black and blue curves. pVar is the percentage variance explained by the MCA mode in **b**–**e**. The spatial pattern correlation coefficient is 0.81 between **b** and **d** and 0.48 between **c** and **e**, both are statistically significant at the 1% level.

the observed global mean surface temperature (Fig. 4a) and the SST MCA1 patterns (Fig. 4c) resemble the observed warming patterns over the oceans[21]. For the same period, the MCA1 from the models show similar nonlinear global warming trends, with ubiquitous warming over the oceans. Associated with this mode, the sc_PDSI_pm, whose short-term variability results mainly from precipitation variations, also exhibits similar temporal evolution (Fig. 4a,b) but with more complex spatial patterns (Fig. 4d,f) that resemble those shown in its trend map (Fig. 1b) for observations. For the models, the global mean warming mode from observations is well captured by the GHG-forced CMIP simulations for both SST and sc_PDSI_pm (Fig. 4a,b), with a correlation of 0.86 and a regression coefficient of 0.9566 between the global mean sc_PDSI_pm anomalies represented by the MCA1 from observations (as the predictor) and the models (as the predictand; Fig. 4a,b). The result suggests that the GHG-forced global aridity changes simulated by the models are consistent with the historical changes.

The MCA1 spatial patterns for sc_PDSI_pm from the models (Fig. 4f) differ considerably from those in observations (Fig. 4d), trend maps (Fig. 2b) and the MCA1 for a longer period from 1950 to 2099 (Fig. 5c). Our analysis of the sc_PDSI_pm from individual models (for example, MCA2 in Supplementary Figs S3 and S4) showed large intermodel variations for this mode for the period from 1923 to 2010 owing to large unforced natural variations and weak GHG-forced signals in precipitation during this time. The trend mode for the sc_PDSI_pm in the individual model runs accounts for only 4–6% of the total variance; they are not robust

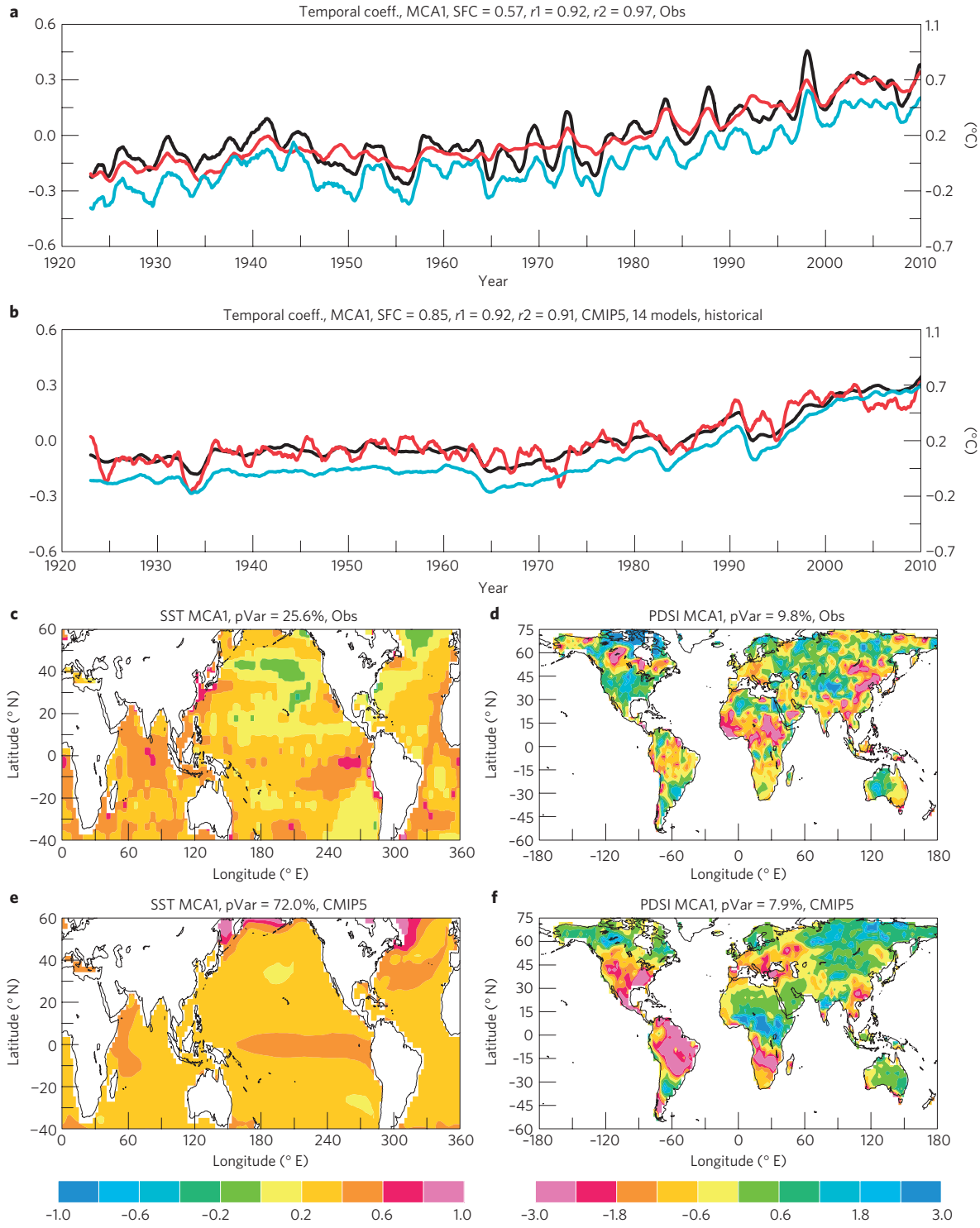

Figure 4 | Temporal and spatial patterns of the MCA1 mode for SST and sc + PDSI_pm from observations and models. a–f, The blue line (right-side ordinate) is the global mean surface temperature from observations[31] in **a** and global mean surface air temperature from the models in **b**, which is the temporal coefficient of the MCA1 for the model SST (black) and sc_PDSI_pm (red). The correlation between the black (red) lines in **a** and **b** is 0.85 (0.86) and the regression coefficient (with the observation as the predictor) between the SST (sc_PDSI_pm) anomalies represented by the MCA1 mode for the observation and models is 0.9119 (0.9566). The product of the temporal (**a,b**) and corresponding spatial (**c–f**) coefficients is the SST and PDSI anomaly represented by the MCA mode, with red areas experiencing warming (for SST) and drying (for PDSI) and blue areas for cooling and wetting.

even for the global mean and less so for individual regions. These results suggest that the global warming mode from observations and individual model runs contain large natural variations unrelated to the historical GHG forcing. In other words, the MCA is unable to completely separate the GHG-forced changes in precipitation and the sc_PDSI_pm from other unforced natural variations because the GHG-forced signal up to 2010 is still relatively weak (only 4–6% of the total variance) compared with the natural variations, especially on regional scales. As most of the natural variations are realization dependent (for example, coupled to initial conditions),

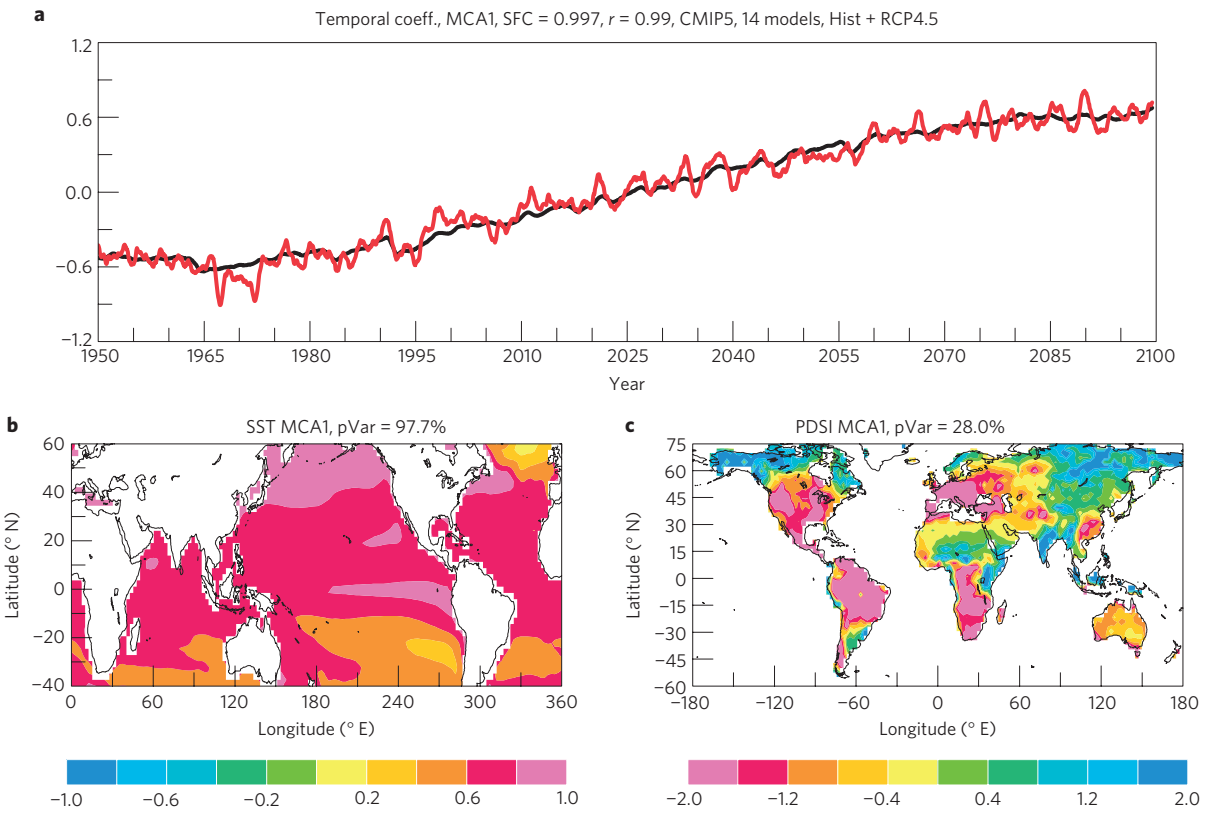

Figure 5 | Temporal and spatial patterns of the CMIP5 model for SST and sc_PDSI_pm from 1950 to 2099 under the RCP4.5 future emissions scenario.

large regional differences between the observations (one single realization) and individual model runs and their ensemble mean are expected. Thus, the differences over West Africa, the USA, Brazil, southern Africa and eastern Australia between Fig. 4d,f probably result from sampling errors among different realizations and natural variations not reproduced by the CMIP model runs.

The differences over the Sahel (10° N–20° N, 18° W–20° E) and the USA in Fig. 4d,f are especially noticeable. The drying trend since 1950 over the Sahel results mainly from the decreases in summer rainfall from the 1950s to the mid-1980s (ref. 22) that are related to the observed large warming in the South Atlantic Ocean relative to the North Atlantic Ocean and the steady warming over the Indian Ocean[8,11], together with significant contributions from dynamic vegetation feedback[23,24], which is not simulated in the CMIP models. Most CMIP3 models produce the opposite warming pattern in the Atlantic Ocean under GHG-induced global warming and thus increasing precipitation over the Sahel in the twenty-first century[11], although a few models do produce some drying over the Sahel under a uniform ocean warming[25]. Supplementary Fig. S5 shows that the HadGEM2-CC and HadGEM2-ES models from the CMIP5 broadly reproduce the observed rainfall decline over the Sahel from the 1950s to 1980s, although with reduced amplitudes, and sulphate aerosols have been identified as the main contributor for this simulated decline in the HadGEM2 models[26]. Apparently, most other CMIP5 models analysed here do not simulate this effect of sulphate aerosols in the twentieth century. For the twenty-first century, the GHG effect will dominate over the aerosol forcing and thus such aerosol-induced drought over the Sahel may not occur again[27]. Nevertheless, the HadGEM2 models still show substantial multidecadal variations in Sahelian rainfall during the twenty-first century (Supplementary Fig. S5).

The wetting trend over the USA results from the upward trend from the 1950s to the 1990s; thereafter, the USA as a whole has become drier (Supplementary Fig. S6a). These multidecadal variations are linked to the Interdecadal Pacific Oscillation (IPO; ref. 28), which switched to a warm phase with above-normal SSTs in the tropical Pacific around 1977 and entered a cold phase around 1999 (refs 19,28; Supplementary Fig. S6b). The IPO has major influences on US precipitation and drought, especially over the southwest USA (ref. 28; Supplementary Fig. S6). As the IPO cycles in the twentieth century (Supplementary Fig. S6b) do not follow any known anthropogenic forcing, to a large extent they are likely to be unforced natural cycles that depend on the initial conditions of the coupled models and thus are generally irreproducible.

The above analysis suggests that the differences between Fig. 4d,f are mainly due to model deficiencies in simulating the effects of sulphate aerosols in the twentieth century, natural SST variations not captured by the CMIP models and sampling errors among different realizations as the GHG-forced signal in sc_PDSI_pm is still relatively weak up to now. Taking these factors into account, the overall resemblance of the MCA1 and MCA2—the only two statistically significant modes—between the observations and the model simulations has important implications. It suggests that the global warming mode in the observations is likely to be part of the GHG-induced warming mode that will become more evident in a few more decades (Fig. 5a); the models are capable of capturing not only the GHG-induced trend mode (MCA1) seen in observations (for the global mean only) so far, but also the main physical, ENSO-like mode (MCA2), which increases our confidence in the model predictions; and increasing drought (Figs 5c and 2b) may be likely over most of the Americas, southern Europe, southern and central Africa, Australia and southeast Asia as the GHG-induced warming continues in the twenty-first century, although the ability of the models to simulate the precipitation and PDSI changes over these regions has yet to be validated. However, the MCA1 patterns (Fig. 5c) for sc_PDSI_pm for the twenty-first century are fairly

stable among the models because of the large forced trend compared with natural variations in temperature, precipitation and other variables. They suggest severe drought conditions by the late half of this century over many densely populated areas such as Europe, the eastern USA, southeast Asia and Brazil. This dire prediction could have devastating impacts on a large number of the population if the model's regional predictions turn out to be true.

Methods

The method and historical forcing data used to compute the sc_PDSI_pm are described by ref. 2. Ref. 2 also provides a detailed description of the caveats of the PDSI and an evaluation of the sc_PDSI_pm. It shows that the sc_PDSI_pm is significantly correlated with observations of soil moisture over the former Soviet Union, Mongolia, China and the USA, with streamflow data over the world's main river basins, and with satellite observations of water storage changes over all land areas. In particular, the correlations do not differ greatly over the US and other regions, including the high-latitude and tropical land areas. These results suggest that the sc_PDSI_pm can be used as a measure of large-scale annual aridity changes over global land areas including the cold regions, despite the simplicity of the PDSI model in treating many land-surface processes such as vegetation and snow cover.

Ref. 2 compares the impact of two different parameterizations of the potential evapotranspiration on the PDSI and finds that the PDSI with the Penman–Monteith potential evapotranspiration (sc_PDSI_pm) showed slightly reduced drying trends from 1950 to 2008 compared with that using the Thornthwaite potential evapotranspiration. For model-predicted twenty-first-century climates, the use of the Penman–Monteith potential evapotranspiration greatly reduces the drying trend[1].

I used the Hadley Centre Sea Ice and Sea Surface Temperature data set data set[29] in the MCA analysis. The MCA is a standard singular value decomposition method[17] that is useful for exploring relationships between two separate fields, although physical interpretations of the MCA modes require additional knowledge. The analysis here focused on the period from 1923 onward, as tropical SST and other data for earlier years are less reliable. The CMIP3 (used for Intergovernmental Panel on Climate Change Fourth Assessment Report; ref. 21) and new CMIP5 model simulations were downloaded from http://cmip-pcmdi.llnl.gov/. I used only one ensemble run from the historical and future simulations for each model and the intermediate GHG emissions scenario Special Report on Emissions Scenarios A1B (for CMIP3) and Representative Concentration Pathway 4.5 (RCP4.5) (for CMIP5) were used (see http://www.ipcc.ch/ipccreports/sres/emission/index.php?idp=14 for more details). I used data from 14 CMIP5 models with data available in November 2011 and most (22) of the CMIP3 models. The 14 CMIP5 models are CNRM-CM5, CSIRO-Mk3-6-0, CanESM2, GISS-E2-R, HadGEM2-CC, HadGEM2-ES, IPSL-CM5A-LR, MIROC-ESM, MIROC-ESM-CHEM, MIROC4h, MIROC5, MPI-ESM-LR, MRI-CGCM3 and inmcm4. Only 11 of these models provided soil-moisture data (13 for CMIP3 models). I used the multimodel ensemble-averaged data in the MCA and change analysis, except stated otherwise (for example, in Supplementary Figs S3 and S4).

Received 30 April 2012; accepted 25 June 2012; published online 5 August 2012; corrected online 22 January 2013

References

1. Dai, A. Drought under global warming: A review. *WIREs Climatic Change* **2,** 45–65 (2011).
2. Dai, A. Characteristics and trends in various forms of the Palmer Drought Severity Index (PDSI) during 1900–2008. *J. Geophys. Res.* **116,** D12115 (2011).
3. Wang, G. L. Agricultural drought in a future climate: Results from 15 global climate models participating in the IPCC 4th assessment. *Clim. Dynam.* **25,** 739–753 (2005).
4. Sheffield, J. & Wood, E. F. Projected changes in drought occurrence under future global warming from multi-model, multi-scenario, IPCC AR4 simulations. *Clim. Dynam.* **31,** 79–105 (2008).
5. Rind, D., Goldberg, R., Hansen, J., Rosenzweig, C. & Ruedy, R. Potential evapotranspiration and the likelihood of future drought. *J. Geophys. Res.* **95,** 9983–10004 (1990).
6. Burke, E. J. & Brown, S. J. Evaluating uncertainties in the projection of future drought. *J. Hydrometeorol.* **9,** 292–299 (2008).
7. Seager, R. *et al.* Model projections of an imminent transition to a more arid climate in southwestern North America. *Science* **316,** 1181–1184 (2007).
8. Giannini, A., Saravanan, R. & Chang, P. Oceanic forcing of Sahel rainfall on interannual to interdecadal time scales. *Science* **302,** 1027–1030 (2003).
9. Schubert, S. D., Suarez, M. J., Pegion, P. J., Koster, R. D. & Bacmeister, J. T. On the cause of the 1930s Dust Bowl. *Science* **303,** 1855–1859 (2004).
10. Seager, R., Kushnir, Y., Herweijer, C., Naik, N. & Velez, J. Modeling of tropical forcing of persistent droughts and pluvials over western North America: 1856–2000. *J. Clim.* **18,** 4065–4088 (2005).
11. Hoerling, M., Hurrell, J., Eischeid, J. & Phillips, A. Detection and attribution of twentieth-century northern and southern African rainfall change. *J. Clim.* **19,** 3989–4008 (2006).
12. Schubert, S. *et al.* A US CLIVAR project to assess and compare the responses of global climate models to drought-related SST forcing patterns: Overview and results. *J. Clim.* **22,** 5251–5272 (2009).
13. Hoerling, M., Eischeid, J. & Perlwitz, J. Regional precipitation trends: Distinguishing natural variability from anthropogenic forcing. *J. Clim.* **23,** 2131–2145 (2010).
14. Burke, E. J. Understanding the sensitivity of different drought metrics to the drivers of drought under increased atmospheric CO_2. *J. Hydrometeorol.* **12,** 1378–1394 (2011).
15. Cook, E. R. *et al.* Asian monsoon failure and megadrought during the last millennium. *Science* **328,** 486–489 (2010).
16. van der Schrier, G., Briffa, K. R., Jones, P. D. & Osborn, T. J. Summer moisture variability across Europe. *J. Clim.* **19,** 2818–2834 (2006).
17. Dai, A. G., Qian, T. T., Trenberth, K. E. & Milliman, J. D. Changes in continental freshwater discharge from 1948 to 2004. *J. Clim.* **22,** 2773–2792 (2009).
18. Bretherton, C. S., Smith, C. & Wallace, J. M. An intercomparison of methods for finding coupled patterns in climate data. *J. Clim.* **5,** 541–560 (1992).
19. Deser, C., Phillips, A. S. & Hurrell, J. W. Pacific interdecadal climate variability: Linkages between the tropics and the North Pacific during boreal winter since 1900. *J. Clim.* **17,** 3109–3124 (2004).
20. Dai, A. & Wigley, T. M. L. Global patterns of ENSO-induced precipitation. *Geophys. Res. Lett.* **27,** 1283–1286 (2000).
21. IPCC *Climate Change 2007: The Physical Science Basis.* (Cambridge Univ. Press, 2007).
22. Dai, A., Lamb, P. J., Trenberth, K. E., Hulme, M., Jones, P. D. & Xie, P. The recent Sahel drought is real. *Int. J. Climatol.* **24,** 1323–13331 (2004).
23. Zeng, N., Neelin, J. D., Lau, K. M. & Tucker, C. J. Enhancement of interdecadal climate variability in the Sahel by vegetation interaction. *Science* **286,** 1537–1540 (1999).
24. Wang, G., Eltahir, E. A. B., Foley, J. A., Pollard, D. & Levis, S. Decadal variability of rainfall in the Sahel: results from the coupled GENESIS-IBIS atmosphere-biosphere model. *Clim. Dynam.* **22,** 625–637 (2004).
25. Held, I. M., Delworth, T. L., Lu, J., Findell, K. L. & Knutson, T. R. Simulation of Sahel drought in the 20th and 21st centuries. *Proc. Natl Acad. Sci. USA* **102,** 17891–17896 (2005).
26. Ackerley, D *et al.* Sensitivity of twentieth-century Sahel rainfall to sulfate aerosol and CO_2 forcing. *J. Clim.* **24,** 4999–5014 (2011).
27. Cook, K.H. & Vizy, E. K. Coupled model simulations of the West African monsoon system: Twentieth- and twenty-first-century simulations. *J. Clim.* **19,** 3681–3703 (2006).
28. Dai, A. The influence of the Inter-decadal Pacific Oscillation on US precipitation during 1923–2010. *Clim. Dynam.*, revised; available from http://www.cgd.ucar.edu/cas/adai/publication-dai.html (2012).
29. Rayner, N. A. *et al.* Global analyses of sea surface temperature, sea ice, and night marine air temperature since the late nineteenth century. *J. Geophys. Res.* **108,** 4407 (2003).
30. Zhao, W. N. & Khalil, M. A. K. The relationship between precipitation and temperature over the contiguous United-States. *J. Clim.* **6,** 1232–1236 (1993).
31. Brohan, P., Kennedy, J.J., Harris, I., Tett, S.F.B. & Jones, P.D. Uncertainty estimates in regional and global observed temperature changes: A new dataset from 1850. *J. Geophys. Res.* **111,** D12106 (2006).

Acknowledgements

The author is grateful to the modelling groups and the CMIP projects for making the model data available. This study was partly supported by NCAR's Water Systems Program.

Additional information

Supplementary information is available in the online version of the paper. Reprints and permissions information is available online at www.nature.com/reprints.

Competing financial interests

The author declares no competing financial interests.

ERRATUM

Increasing drought under global warming in observations and models

Aiguo Dai

Nature Clim. Change **3,** 52–58 (2013); published online 5 August 2012; corrected after print 22nd January 2013.

In the version of this Letter originally published, in the sentence beginning "As SSTs have large influences on land precipitation…", the latitude range of sc_PDSI_pm included in the maximum covariance analysis should have read 60° S–75° N. This error has now been corrected in the HTML and PDF versions (note that the 'corrected after print' date in these online versions differs from that given in print).